Enhancement of Passive Scalar Mixing in a Shear-Free Turbulent Front

Tomoaki Watanabe(✉)

Department of Mechanical Engineering and Science, Kyoto University, Kyoto 615-8540, Japan
watanabe.tomoaki.8x@kyoto-u.ac.jp

Abstract. A localized turbulent region expands spatially by entraining surrounding non-turbulent fluid, demarcated by the turbulent/non-turbulent interface (TNTI) layer. Small-scale vortex tubes and shear layers within this TNTI layer play a pivotal role in the process of entrainment. Shear layers in turbulence are known to be unstable against perturbations with wavelengths approximately 30 times the Kolmogorov scale. This study conducts numerical experiments aimed at investigating the potential for enhancing passive scalar mixing through the excitation of small-scale shear instability. Direct numerical simulations (DNS) are conducted for a turbulent front with a passive scalar transfer evolving in the absence of mean shear, where solenoidal velocity perturbations of constant wavelength are introduced outside the turbulent region. These perturbations are found to enhance the entrainment rate significantly when their wavelength coincides with the unstable mode of shear layers. Despite the increased entrainment rate facilitated by the excitation of small-scale shear instability, passive scalar statistics dominated by large-scale scalar distributions, such as mean scalar and root-mean-squared scalar fluctuations, remain largely unaffected. However, this enhanced entrainment rate results in the amplification of the scalar dissipation rate, which provides a measure of scalar mixing at small scales. These findings indicate that exciting small-scale shear instability can effectively enhance entrainment and small-scale scalar mixing in intermittent turbulent flows.

Keywords: Turbulent/non-turbulent interface · Entrainment · Turbulent mixing

1 Introduction

Turbulent entrainment refers to the process by which turbulent flow draws in surrounding non-turbulent fluid. This phenomenon is prevalent in canonical turbulent flows, such as jets, wakes, and boundary layers, which exhibit large-scale intermittency. At a fixed location within these flows, regions of turbulent and non-turbulent fluids are intermittently observed. A thin interface layer,

J. Wang and I. Marusic (Eds.): IUTAM-TNTI 2024, IUTAM Bookseries 45, pp. 79–93, 2025.
https://doi.org/10.1007/978-3-031-78151-3_6

known as the turbulent/non-turbulent interface (TNTI), demarcates the turbulent region from the non-turbulent fluid. The TNTI layer is characterized by its minimal thickness, which scales with the Kolmogorov scale, and exhibits a complex geometry shaped by turbulent motions across a broad range of length scales [1]. The structure of the TNTI layers has been analyzed through two- or three-dimensional velocity measurements utilizing particle image velocimetry and direct numerical simulations (DNS) [2,3]. The TNTI layer comprises an outer viscous superlayer and an inner turbulent sublayer. The turbulent and non-turbulent regions can be distinguished by the presence of vorticity, $\boldsymbol{\omega} = \nabla \times \boldsymbol{u}$. Turbulent entrainment is thus conceptualized as a mechanism through which non-turbulent fluid acquires enstrophy, $\omega^2/2 = (\boldsymbol{\omega} \cdot \boldsymbol{\omega})/2$, within the TNTI layer [4,5]. In the viscous superlayer, the growth of $\omega^2/2$ is attributed to viscous diffusion from the turbulent sublayer, while the contribution of inviscid vortex stretching to enstrophy amplification is considered negligible. Conversely, vortex stretching significantly enhances enstrophy within the turbulent sublayer. This transport of enstrophy within the TNTI layer is elucidated by the presence of small-scale vortical structures, such as vortex tubes and sheets, within the turbulent sublayer [6–10]. These structures, characterized by high enstrophy, facilitate an outward viscous diffusion of enstrophy. Moreover, the production of enstrophy via vortex stretching occurs within these structures [6,11,12]. Vortex tubes and sheets play a pivotal role in the process of entrainment.

The TNTI layer also plays a crucial role in scalar mixing [13]. In scenarios where two chemicals are introduced separately into turbulent and non-turbulent flows, the mixing and subsequent chemical reactions are primarily facilitated by the entrainment of the non-turbulent fluid [14–16]. A significant scalar concentration gradient is observed within the TNTI layer, particularly in the direction normal to the interface [17–20]. This pronounced gradient drives the transfer of scalar concentrations by molecular diffusion between the turbulent and entrained fluids. While molecular diffusion tends to smooth the scalar profile within the TNTI layer, the process of inertial scalar transport from the turbulent core region sustains a steep scalar gradient within the TNTI layer [21,22]. These early studies have led to recent investigations of turbulent mixing near the TNTI layer in more complex flows, such as turbulent combustion [23] and buoyant plumes [24]. The analysis of scalar transport near the TNTI layer in jet flames has elucidated the role of the local entrainment process in flame stabilization [25]. Additionally, the nucleation of oil droplets in a jet flow was detailed through concentration measurements in the vicinity of the TNTI layer [26].

Turbulence has been examined from a structural perspective, revealing that at small scales, high enstrophy regions are found within tubular or sheet-like structures, known as vortex tubes and sheets, respectively [11,27]. Various methods have been developed to identify vortex tubes, with one approach identifying them as regions exhibiting large positive values of the second invariant of a velocity gradient tensor [28]. The dimensions of vortex tubes are generally determined by the Kolmogorov scale [6,11]. For many vortex tubes, the relationship between the diameter and the local vortex stretching rate closely aligns

with predictions by the Burgers' vortex model. Vortex sheets, characterized by intense shear and referred to as shear layers, have received comparatively less attention due to identification challenges [29]. Recent advancements in the study of shear layers employ a triple decomposition [30,31]. This decomposition is relevant to the Rortex-based decomposition [32] and Schur decomposition [33]. These methods separate three motions of shear, rigid-body rotation, and irrotational strain (elongation) from the velocity gradient tensor. Shear layers are identifiable through the intensity of shearing motion [12,34]. Recent studies using this decomposition have elucidated the statistical properties of shear layers. Similar to vortex tubes, the thickness of shear layers scales with the Kolmogorov scale [12,35,36]. Additionally, the relationship between the thickness and vortex stretching rate aligns with Burgers' vortex layers. Similar layer structures appear in turbulence as regions with a high scalar dissipation rate. However, it has been shown that shear layers are irrelevant to strongly dissipative regions of passive scalar fluctuations [36]. The velocity field induced by shear layers can be reconstructed using the Biot-Savart law applied to the shear component of vorticity vectors. Analyses of reconstructed velocity fields have demonstrated that shear layers significantly contribute to the energy cascade [37]. Shear layers appear near vortex tubes, and their interaction can be crucial in the formation of a biaxial strain acting on the shear layers [38,39]. Due to the strain and shear, vortex stretching actively occurs in the shear layers [12,40]. These investigations have confirmed the importance of shear layers in various turbulence properties.

Shear layers in turbulence are inherently unstable and shear instability produces vortex tubes [12,41]. Numerical simulations were performed for an isolated shear layer, modeled with the mean flow pattern observed around shear layers in turbulence [42]. Even in the absence of external perturbations, the shear layer exhibits inherent instability due to self-induced velocity from shear vorticity, particularly when the layer possesses a small aspect ratio. This stands in contrast to a uniform shear layer with an infinite aspect ratio, which remains stable in the absence of perturbations. The formation of a vortex from a shear layer with a finite aspect ratio is promoted under the influence of perturbations of a specific wavelength. Coupled with observations of shear layers in turbulence, these findings suggest that the instability of many shear layers in turbulence is excited by perturbations with a wavelength approximately 30 times the Kolmogorov scale. Furthermore, the response of shear layers to such perturbations was investigated through DNS of decaying isotropic turbulence [42]. Upon the influence of perturbations near this critical wavelength, numerous shear layers collapse rapidly, leading to an increased number density of vortex tubes. This rise in the number of vortex tubes, in turn, results in a greater number density of shear layers, which form around the vortex tubes [39].

These investigations into entrainment and the instability of shear layers suggest that stimulating shear instability near the TNTI layer could lead to enhanced passive scalar mixing, alongside the process of entrainment. This study aims to explore the potential for enhancing mixing by introducing perturbations with a wavelength corresponding to the unstable mode of shear layers. For this

purpose, DNS is performed for a shear-free turbulent front with passive scalar transfer. Perturbations are introduced in the non-turbulent region, affecting the entrainment process from outside of turbulence. It will be shown that entrainment and small-scale scalar mixing are enhanced when the perturbations have a wavelength matching the small-scale shear instability.

The flow setup in this study will aid in understanding the modulation of the TNTI layer. In particle-laden flows, particles can disturb the flow field, and recent studies have explored the modulations of the TNTI layer by solid particles [43]. The small-scale shear instability within the TNTI layer may be relevant to particle effects on turbulent entrainment when the particle size matches the unstable wavelength of the shear layers. Additionally, the unstable mode of shear layers within the TNTI layer can be important for the interface between two different turbulent regions, known as a turbulent/turbulent interface (TTI) layer. The TTI layer forms along the shear layers, and entrainment by a primary turbulent region from background turbulence is expected to be influenced by these shear layers [44]. Vortex stretching actively occurs within the shear layers, thus enstrophy production is not negligible within the entire TTI layer, unlike the viscous superlayer for the TNTI layer [45]. Recent investigations of the TTI layer have revealed that background turbulence alters the interface geometry and the entrainment rate of primary turbulence [46–49]. These studies often consider large-scale background turbulence whose integral scale is comparable to that of primary turbulence. The present findings are applicable to understanding the impact of small-scale background turbulence on entrainment and scalar mixing. The characteristic velocity of shear layers is the Kolmogorov velocity scale, which decreases as the Reynolds number increases. Therefore, even weak perturbations can excite its instability at a high Reynolds number as long as the perturbation wavelength matches the instability mode [42]. This feature can be important in establishing control strategies for turbulent entrainment. Therefore, shear instability within the TNTI layer has many potential applications in engineering fields, such as flows around airfoils [50] and turbulent combustion [25]. Controlling entrainment with small-scale disturbance might also be important in meteorological fields, where small-scale instability might be leveraged to control atmospheric phenomena with small-scale and weak disturbances from human activity [51]. For example, cloud evolutions are often influenced by the entrainment process at the edge, which has recently been studied in terms of the TNTI layer [52,53].

2 DNS of a Shear-Free Turbulent Front Subject to External Perturbations

2.1 A Shear-Free Turbulent Front

DNS is conducted for a shear-free turbulent front with passive scalar transfer [54,55]. The flow is initiated by introducing homogeneous isotropic turbulence (HIT) into a quiescent fluid. This setup allows the turbulent region to expand

by entraining the surrounding non-turbulent fluid, without being influenced by mean shear. The computational domain is configured as a cube with dimensions L^3, discretized into N^3 grid points. The incompressible Navier–Stokes equations, coupled with the advection-diffusion equation for a passive scalar ϕ, govern the flow evolution. These equations are expressed as follows:

$$\frac{\partial u_j}{\partial x_j} = 0, \tag{1}$$

$$\frac{\partial u_i}{\partial t} + \frac{\partial u_i u_j}{\partial x_j} = -\frac{1}{\rho}\frac{\partial p}{\partial x_i} + \nu \frac{\partial^2 u_i}{\partial x_j \partial x_j}, \tag{2}$$

$$\frac{\partial \phi}{\partial t} + \frac{\partial u_j \phi}{\partial x_j} = D \frac{\partial^2 \phi}{\partial x_j \partial x_j}, \tag{3}$$

where x_i denotes position, t time, u_i the velocity vector, p pressure, ρ density, and ν the kinematic viscosity. The diffusivity coefficient for ϕ is represented by D. The Schmidt number, $Sc = \nu/D$, is assumed to be unity. These equations are solved using an in-house finite-difference code based on the fractional step method [12]. Spatial and temporal discretizations employ the fourth-order fully conservative central difference and third-order Runge–Kutta schemes, respectively [56]. The Poisson equation for pressure is solved using the BiCGStab method.

The initial velocity field for the shear-free turbulent front is generated by applying a top-hat function $C(y)$ to the velocity field HIT, $\boldsymbol{u}_{HIT}$, resulting in $C\boldsymbol{u}_{HIT}$:

$$C(y) = 0.5 + 0.5\tanh\left[\frac{4}{\Delta_I}\left(1 - \frac{2|y - L/2|}{L_T}\right)\right], \tag{4}$$

where $C(y) = 1$ closely approximates the central region $|y| \lesssim L_T/2$ and $C(y) = 0$ elsewhere. This configuration ensures statistical homogeneity along the x and z directions, with a distinct interface perpendicular to the y direction. The coordinate system (x, y, z) is defined with $y = 0$ at the domain center and $(x, z) = (0, 0)$ at the corner of the x–z plane. The statistical properties of HIT are evaluated using a volume average denoted by $\overline{f}$ for any variable f, with $f' = f - \overline{f}$ representing its fluctuating component. The average kinetic energy dissipation rate is $\varepsilon = \overline{2\nu S_{ij} S_{ij}}$, where $S_{ij} = (\partial u_i/\partial x_j + \partial u_j/\partial x_i)/2$ is the rate-of-strain tensor. The Kolmogorov length, time, and velocity scales are defined as $\eta = (\nu^3/\varepsilon)^{1/4}$, $\tau_\eta = (\nu/\varepsilon)^{1/2}$, and $u_\eta = (\nu\varepsilon)^{1/4}$, respectively. Subscript 0 indicates initial HIT statistics, such as η_0 and $u_{\eta 0}$. The initial turbulent region has a width of $L_T = L/3$ and the interfacial layer thickness of $\Delta_I = 10\eta_0$. The initial scalar profile is given by $\phi = C(y)$, distinguishing the turbulent region ($\phi > 0$) from the exterior ($\phi = 0$).

The DNS database of statistically steady HIT subject to a linear forcing [57] is used to generate the initial field. The simulation parameters were determined to realize HIT with the time-averaged Reynolds number $Re_{L0} = u_{rms0} L_{I0}/\nu = 350$, where $u_{rms} = \sqrt{\overline{u'^2}}$ is the root-mean-squared (rms) velocity fluctuation and L_I

is the characteristic length scale of large-scale motion defined as $L_I = u_{rms}^3/\varepsilon$. The computational domain size L^3 is $(5.3L_{I0})^3$ based on the time average of L_{I0} of HIT. Five snapshots are used as the initial conditions of the turbulent front. Based on ensemble averages, the turbulent Reynolds number $Re_\lambda = u_{rms}\lambda/\nu$ defined with the Taylor microscale $\lambda = \sqrt{15\nu u_{rms}^2/\varepsilon}$ and the rms velocity fluctuations is $Re_{\lambda 0} = 72$. The number of grid points N^3 is 512^3, for which the grid spacing $\Delta = L/N$ is $0.8\eta_0$. The subsequent simulation of the turbulent front also uses the same computational parameters by modifying the velocity field of HIT with Eq. (4). As the turbulent front decays, η increases with time, ensuring that Δ is smaller than 0.8η. Figure 1 shows the two-dimensional distributions of ϕ, visualizing the temporal evolution of the shear-free turbulent front. The turbulent region with $\phi > 0$ spatially expands with time by entraining the external fluid with $\phi = 0$.

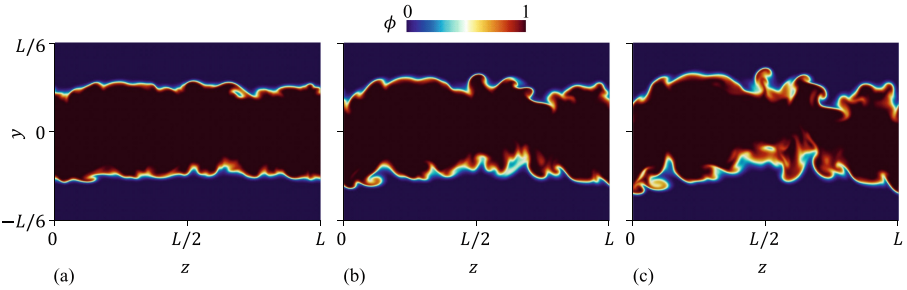

Fig. 1. Development of the shear-free turbulent front without perturbations. Two-dimensional distributions of the passive scalar ϕ are visualized at (a) $t = 2\tau_{\eta 0}$, (b) $t = 4\tau_{\eta 0}$, and (c) $t = 6\tau_{\eta 0}$.

This study delves into the effects of introducing perturbations external to the turbulent region. Building on insights from a prior investigation of the perturbation response of decaying HIT [42], solenoidal perturbations are superimposed on the initial velocity field. These perturbations are represented by sinusoidal functions as follows:

$$\boldsymbol{u}_P = (1 - C)\left[u_f \sin(2\pi y/\lambda_f), u_f \sin(2\pi z/\lambda_f), u_f \sin(2\pi x/\lambda_f)\right], \tag{5}$$

where the amplitude u_f and the wavelength λ_f define the perturbation characteristics. Given the nature of $C(y)$, the influence of $\boldsymbol{u}_P$ sharply declines from the outside towards the turbulent region. Perturbation parameters u_f and λ_f are determined based on $u_{\eta 0}$ and η_0, respectively. The study considers two values for λ_f: $\lambda_f = 30\eta_0$, corresponding to the unstable mode of shear instability, and $\lambda_f = 140\eta_0$, which is unrelated to the instability. Prior work has assessed the role of u_f in exciting shear instability within HIT [42]. The perturbation effects are determined by the ratio of u_f to $u_{\eta 0}$ for $\lambda_f \approx 30\eta_0$. Herein, u_f is set at $u_f/u_{\eta 0} = 1.4$. In addition to these perturbed cases, a shear-free turbulent

front without of perturbations is also simulated as a reference case for comparative analysis. The influence of the perturbations is elucidated by comparing the perturbed cases with the unperturbed baseline. The simulation time spans over $10\tau_{\eta 0}$. Notably, the perturbation effects on shear instability in decaying HIT were shown to prevail within a few times the Kolmogorov time scale [42]. The shear-free turbulent front exhibits statistical homogeneity on the x–z planes, and spatial averages across the x–z planes are taken as functions of y and t. In addition, ensemble averages are taken for five simulations initialized with different snapshots of HIT.

Compared to other turbulent shear flows, shear-free turbulence offers the advantage of initial statistical homogeneity within the turbulent region. A critical parameter in the present DNS is the ratio of the perturbation wavelength λ_f to the Kolmogorov scale η. Given that η remains constant within the initial turbulent region, adopting a constant λ_f ensures that the ratio λ_f/η is also constant. In contrast, in turbulent shear flows, η and other length scales vary spatially within the turbulent region, complicating the interpretation of results based on the ratio between the perturbation wavelength and turbulence length scales. Previous studies have demonstrated that the characteristics of the TNTI and small-scale shear layers are largely unaffected by mean shear [10,58]. Although the present DNS excludes mean shear effects, the findings are anticipated to be relevant for more complex flows with mean shear, such as jets and mixing layers.

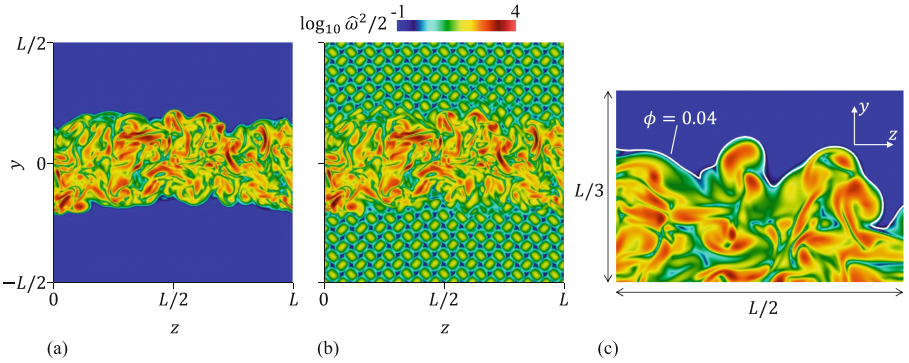

Fig. 2. Enstrophy distributions at $t = 4\tau_{\eta 0}$ in (a) the unperturbed case and (b) the perturbed case with $\lambda_f = 30\eta_0$. (c) The iso-scalar line of $\phi = 0.04$ and enstrophy distribution near the TNTI layer at $t = 7\tau_{\eta 0}$. Enstrophy is normalized as $\hat{\omega}^2/2 = (\omega^2/2)/(u_{rms0}^2/L_0^2)$.

2.2 The Evaluation of the Entrainment Rate with Isosurface Area Density

The entrainment rate is quantified by examining the boundary propagation of the turbulent front. Figure 2 depicts the two-dimensional distributions of enstrophy, $\omega^2/2$, in the turbulent front, both with and without the introduction of initial perturbations. As outlined in Eq. (5), vortical perturbations result in a spatially periodic variation in enstrophy, which is notably apparent outside the turbulent front in Fig. 2(b). Consequently, enstrophy is deemed unsuitable for the identification of the TNTI layer, which is more accurately identified using the passive scalar. Previous research has demonstrated that enstrophy and passive scalar isosurfaces, for $Sc = 1$, align closely in terms of their location and shape at the outer edge of the TNTI layer [17,59]. The outer boundary of the TNTI layer is determined by an isosurface of $\phi = \phi_{th}$, for which the turbulent front is defined by $\phi > \phi_{th}$. Here, $\phi_{th} = 0.04$ is selected based on the threshold dependence of the turbulent volume [60]. For the unperturbed case, Fig. 2 compares the iso-scalar line of $\phi = \phi_{th}$ and the enstrophy distribution. The iso-scalar line precisely delineates the boundary between rotational and irrotational fluids. The TNTI layer encompasses both the outer viscous superlayer and the inner turbulent sublayer, with the isosurface of ϕ residing at the outer boundary of the viscous superlayer, adjacent to the irrotational fluid. Thus, this isosurface is referred to as the irrotational boundary [21].

The entrainment rate is calculated as the surface integral of the propagation velocity of the irrotational boundary. This calculation is performed for a specific time step to derive the entrainment rate as a function of time. The surface integral is computed using an isosurface area density, Σ', as detailed by Blakeley et al. [61]. The function $X(x, y, z)$, serving as an indicator of the turbulent front, is defined by:

$$X = \begin{cases} 1 & \text{outside the turbulent front } (\phi(x,y,z) \leq \phi_{th}) \\ 0 & \text{inside the turbulent front } (\phi(x,y,z) > \phi_{th}) \end{cases}. \tag{6}$$

The isosurface area density for the scalar isosurface of $\phi(x, y, z) = \phi_{th}$ is specified as follows:

$$\Sigma'(x,y,z) = -\frac{1}{\sqrt{(\partial\phi/\partial x_i)^2}} \frac{\partial X}{\partial x_j} \frac{\partial \phi}{\partial x_j}. \tag{7}$$

The total area of the isosurface within the computational domain $\mathcal{V}$ is calculated by the volume integral of the isosurface area density, $A = \iiint_{\mathcal{V}} \Sigma' dxdydz$. For any function f, its surface integral, denoted as $\langle f \rangle_S$, is written with a volume integral, $\langle f \rangle_S = \iiint_{\mathcal{V}} f\Sigma' dxdydz$. The propagation velocity of a scalar isosurface at a point (x, y, z) is determined as $v_P(x, y, z) = |\nabla\phi|^{-1} D\nabla^2\phi$, with the propagation direction represented by $\boldsymbol{n} = -\nabla\phi/|\nabla\phi|$. The volume of the turbulent front, V_T, is obtained by integrating $(1 - X)$ over the domain, $V_T = \iiint_{\mathcal{V}} (1 - X) dxdydz$. The entrainment rate, $\dot{V}_T$, quantifies the temporal change in V_T and is defined through the surface integral of v_P on the irrotational boundary as $\dot{V}_T = \langle v_P \rangle_S$.

Positive $\dot{V}_T$ values signify the expansion of the turbulent front by entraining external fluid.

3 Results and Discussion

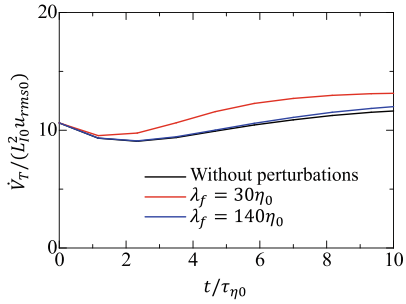

Fig. 3. Temporal variations of entrainment rate $\dot{V}_T$.

Figure 3 presents the temporal variation in the entrainment rate, $\dot{V}_T$, comparing the cases with and without perturbations over time. Initially, for $t/\tau_{\eta 0} \lesssim 1$, the entrainment rate appears consistent across all cases. The introduction of perturbations with $\lambda_f = 30\eta_0$ notably increases $\dot{V}_T$ in comparison to the unperturbed case. Conversely, the entrainment rate remains largely unchanged in the presence of perturbations with $\lambda_f = 140\eta_0$, despite an identical perturbation amplitude of $u_f = 1.4u_{\eta 0}$ to that in the $\lambda_f = 30\eta_0$ case. The differential impact of these perturbations was previously explored in isotropic turbulence through the visualization of shear layers and the assessment of the number of vortices [42]. Perturbations with $\lambda_f = 30\eta_0$ were shown to promote shear instability, leading to rapid vortex formation. It was also shown that shear layers exhibit minimal response to perturbations with a wavelength irrevent to the shaer instability. Perturbations effectively influence entrainment when their wavelength aligns with the unstable mode of shear instability. For the present case, the perturbations of $\lambda_f = 30\eta_0$ elevate the entrainment rate by 17% relative to the unperturbed case, underscoring the pivotal role of small-scale vortices and shear layers in the entrainment mechanism.

The above investigations reveal that entrainment is effectively promoted by perturbations when the wavelength aligns with the unstable mode of shear instability. The consequences of the entrainment enhancement on scalar mixing are assessed through passive scalar statistics. Figure 4(a) presents the lateral distribution of the mean scalar, $\overline{\phi}$, across three time instances, showcasing the evolution of a scalar mixing layer within the turbulent front. The scalar mixing layer, characterized by $0 < \overline{\phi} < 1$, broadens in the y direction over time. Notably, despite the increase in the entrainment rate, the profile of $\overline{\phi}$ remains largely consistent, irrespective of perturbations. Figure 4(b) shows the profile of rms scalar

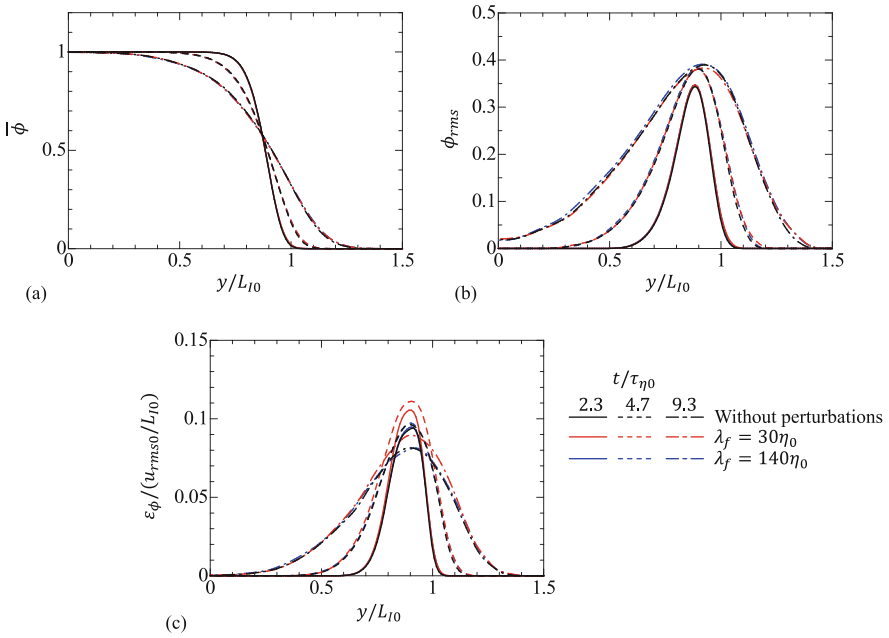

Fig. 4. Lateral distributions of (a) mean scalar $\overline{\phi}$, (b) rms scalar fluctuations ϕ_{rms}, and (c) averaged dissipation rate of scalar fluctuations ε_ϕ.

fluctuations, $\phi_{rms} = \sqrt{\overline{\phi'^2}}$. Initially, ϕ_{rms} is zero due to $\phi = C(y)$; however, as the turbulent front develops, scalar fluctuations are generated by the turbulent scalar flux in the y direction, $\overline{v'\phi'}$. This flux contributes to the production term of scalar variance, $-2\overline{v'\phi'}(\partial\overline{\phi}/\partial y)$. Thus, ϕ_{rms} peaks in areas with a significant mean scalar gradient. The expansion of the scalar mixing layer over time results in a spatially broader distribution of ϕ_{rms}. The presence of perturbations appears to have minimal effects on ϕ_{rms}, which exhibits nearly identical profiles for all cases. While perturbations with $\lambda_f = 30\eta_0$ increases the entrainment rate by exciting the shear instability at small scales, they do not alter mean scalar profiles or rms scalar fluctuations significantly, as these scalar statistics are dominated by large-scale scalar distributions. Figure 4(c) exhibits the lateral profile of the averaged dissipation rate of scalar fluctuations, $\varepsilon_\phi = \overline{D\nabla\phi \cdot \nabla\phi}$. Contrary to the behaviors of mean scalar and rms scalar fluctuations, perturbations with $\lambda_f = 30\eta_0$ lead to a pronounced increase in ε_ϕ. This enhancement in scalar dissipation rate is not observed for $\lambda_f = 140\eta_0$. Thus, the entrainment enhancement affects the scalar statistics related to small-scale scalar fluctuations.

The analysis of the scalar energy spectrum provides insights into the scale-dependent effects of perturbations on scalar mixing. The Fourier transform of the scalar field, ϕ, along the x direction and its complex conjugate are represented as $\hat{\phi}(k_x, y, z)$ and $\hat{\phi}^*(k_x, y, z)$, respectively, where k_x is the wavenumber in the x direction. The energy spectrum of ϕ, denoted as $E_\phi(k_x, y)$, is defined as

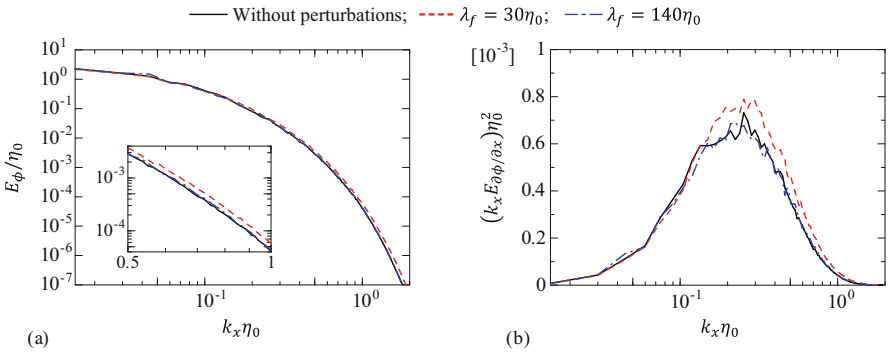

Fig. 5. Energy spectra of (a) scalar fluctuations ϕ', E_ϕ and (b) scalar gradient $\partial\phi/\partial x$, $E_{\partial\phi/\partial x}$ at $t = 8\tau_{\eta 0}$.

$E_\phi(k_x, y) = \mathrm{Re}[\overline{\hat{\phi}\hat{\phi}^*}]$, where Re represents a real part of complex variables and the average is taken spatially in the z direction. This spectrum is specifically evaluated at a position $y/L_{I0} = 0.89$, near the center of the scalar mixing layer.

Figure 5(a) reveals the energy spectrum E_ϕ at $t = 8\tau_{\eta 0}$, a point in time when perturbations have already enhanced both the entrainment and scalar dissipation rates. The introduction of perturbations, irrespective of their wavelength, shows minimal impact on the overall shape of the spectrum. Notably, the spectra at lower wavenumbers (representing large scales) closely align across cases, indicating that perturbations do not significantly alter large-scale scalar distributions. However, the introduction of perturbations with $\lambda_f = 30\eta_0$ leads to an elevated E_ϕ at high wavenumbers compared to the unperturbed case. This influence is not observed for $\lambda_f = 140\eta_0$.

Figure 5(b) presents the energy spectrum of the scalar gradient, $E_{\partial\phi/\partial x}$, premultiplied by the wavenumber, k_x. The premultiplied spectrum is displayed on a semi-logarithmic scale to assess the contribution of each scale to $\overline{(\partial\phi/\partial x)^2}$, which is associated with the scalar dissipation rate. This relationship is expressed as $\overline{(\partial\phi/\partial x)^2} = \int E_{\partial\phi/\partial x} dk_x$ and can be reformulated as $\overline{(\partial\phi/\partial x)^2} = \int k_x E_{\partial\phi/\partial x} d(\log_{10} k_x)$. Thus, the area under the curve of $k_x E_{\partial\phi/\partial x}$ represents the contribution to $\overline{(\partial\phi/\partial x)^2}$ at the scale of $\log_{10} k_x$. Introducing perturbations with $\lambda_f = 30\eta_0$ increases $k_x E_{\partial\phi/\partial x}$ for $k_x\eta_0 \gtrsim 0.15$ compared to the unperturbed case, while no such increase is observed for $\lambda_f = 140\eta_0$. Given that the scalar gradient is predominantly influenced by small-scale scalar fluctuations, this enhancement in $k_x E_{\partial\phi/\partial x}$ reflects a corresponding change in E_ϕ at high wavenumbers, indicating that small-scale scalar fluctuations are amplified with the introduction of perturbations at $\lambda_f = 30\eta_0$. Such perturbations efficiently promote small-scale shear instability, thereby enhancing the entrainment rate. These observations imply that enhanced entrainment promotes rapid scalar mixing at small scales without affecting the large-scale scalar distribution.

4 Conclusions

DNS has been performed to investigate the potential for enhancing passive scalar mixing through the excitation of small-scale shear instability. This study simulates a turbulent front without mean shear, subjected to external perturbations of constant wavelength. When the wavelength corresponds with the unstable mode of shear layers, as documented in previous research [42], the perturbations lead to an increase in the entrainment rate. This enhancement of entrainment does not occur for perturbations with wavelengths irrelevant to the shear instability. The impact of this entrainment enhancement on scalar mixing has been evaluated using passive scalar statistics. The mean scalar profile and rms scalar fluctuations, primarily influenced by large-scale scalar distributions, remain unaffected by the increased entrainment rate. However, the scalar dissipation rate experiences amplification as a result of increased entrainment. This amplification is attributed to enhanced scalar fluctuations at small scales. The characteristics of shear layers are defined by Kolmogorov scales, and the length and velocity scales of the shear layers, normalized by Kolmogorov scales, are consistent across different flows and Reynolds numbers. The findings suggest that small-scale shear instability can be exploited to enhance entrainment and small-scale scalar mixing in various intermittent turbulent flows.

Acknowledgements. Numerical simulations presented in this paper were performed using the high-performance computing systems at the Japan Agency for Marine-Earth Science and Technology and Nagoya University. This work was also supported by a Collaborative Research Project on Computer Science with High-Performance Computing in Nagoya University and by JSPS KAKENHI Grant Number JP22K03903.

References

1. da Silva, C.B., Hunt, J.C.R., Eames, I., Westerweel, J.: Interfacial layers between regions of different turbulence intensity. Annu. Rev. Fluid Mech. **46**, 567–590 (2014)
2. Bisset, D.K., Hunt, J.C.R., Rogers, M.M.: The turbulent/non-turbulent interface bounding a far wake. J. Fluid Mech. **451**, 383–410 (2002)
3. Westerweel, J., Fukushima, C., Pedersen, J.M., Hunt, J.C.R.: Mechanics of the turbulent-nonturbulent interface of a jet. Phys. Rev. Lett. **95**(17), 174501 (2005)
4. Holzner, M., Lüthi, B.: Laminar superlayer at the turbulence boundary. Phys. Rev. Lett. **106**(13), 134503 (2011)
5. Taveira, R.R., da Silva, C.B.: Characteristics of the viscous superlayer in shear free turbulence and in planar turbulent jets. Phys. Fluids **26**(2), 021702 (2014)
6. da Silva, C.B., Dos Reis, R.J.N., Pereira, J.C.F.: The intense vorticity structures near the turbulent/non-turbulent interface in a jet. J. Fluid Mech. **685**, 165–190 (2011)
7. Jahanbakhshi, R., Vaghefi, N.S., Madnia, C.K.: Baroclinic vorticity generation near the turbulent/non-turbulent interface in a compressible shear layer. Phys. Fluids **27**(10), 105105 (2015)

8. Watanabe, T., Jaulino, R., Taveira, R.R., da Silva, C.B., Nagata, K., Sakai, Y.: Role of an isolated eddy near the turbulent/non-turbulent interface layer. Phys. Rev. Fluids **2**(9), 094607 (2017)
9. Neamtu-Halic, M.M., Krug, D., Mollicone, J.P., van Reeuwijk, M., Haller, G., Holzner, M.: Connecting the time evolution of the turbulence interface to coherent structures. J. Fluid Mech. **898**, A3 (2020)
10. Hayashi, M., Watanabe, T., Nagata, K.: The relation between shearing motions and the turbulent/non-turbulent interface in a turbulent planar jet. Phys. Fluids **33**(5), 055126 (2021)
11. Jiménez, J., Wray, A.A.: On the characteristics of vortex filaments in isotropic turbulence. J. Fluid Mech. **373**, 255–285 (1998)
12. Watanabe, T., Tanaka, K., Nagata, K.: Characteristics of shearing motions in incompressible isotropic turbulence. Phys. Rev. Fluids **5**(7), 072601(R) (2020)
13. Westerweel, J., Fukushima, C., Pedersen, J.M., Hunt, J.C.R.: Momentum and scalar transport at the turbulent/non-turbulent interface of a jet. J. Fluid Mech. **631**, 199–230 (2009)
14. Watanabe, T., Sakai, Y., Nagata, K., Ito, Y., Hayase, T.: Reactive scalar field near the turbulent/non-turbulent interface in a planar jet with a second-order chemical reaction. Phys. Fluids **26**(10), 105111 (2014)
15. Cifuentes, L., Kempf, A., Dopazo, C.: Local entrainment velocity in a premixed turbulent annular jet flame. Proc. Combus. Inst. **37**(2), 2493–2501 (2019)
16. Gauding, M., Bode, M., Denker, D., Brahami, Y., Danaila, L., Varea, E.: On the combined effect of internal and external intermittency in turbulent non-premixed jet flames. Proc. Combust. Inst. **38**(2), 2767–2774 (2021)
17. Gampert, M., Boschung, J., Hennig, F., Gauding, M., Peters, N.: The vorticity versus the scalar criterion for the detection of the turbulent/non-turbulent interface. J. Fluid Mech. **750**, 578–596 (2014)
18. Watanabe, T., Riley, J.J., Nagata, K.: Effects of stable stratification on turbulent/nonturbulent interfaces in turbulent mixing layers. Phys. Rev. Fluids **1**(4), 044301 (2016)
19. Mistry, D., Philip, J., Dawson, J.R., Marusic, I.: Entrainment at multi-scales across the turbulent/non-turbulent interface in an axisymmetric jet. J. Fluid Mech. **802**, 690–725 (2016)
20. Kohan, K.F., Gaskin, S.: The effect of the geometric features of the turbulent/non-turbulent interface on the entrainment of a passive scalar into a jet. Phys. Fluids **32**(9), 095114 (2020)
21. Watanabe, T., Sakai, Y., Nagata, K., Ito, Y., Hayase, T.: Turbulent mixing of passive scalar near turbulent and non-turbulent interface in mixing layers. Phys. Fluids **27**(8), 085109 (2015)
22. Watanabe, T., Naito, T., Sakai, Y., Nagata, K., Ito, Y.: Mixing and chemical reaction at high Schmidt number near turbulent/nonturbulent interface in planar liquid jet. Phys. Fluids **27**(3), 035114 (2015)
23. Chakraborty, N., Klein, M., Im, H.G.: A comparison of entrainment velocity and displacement speed statistics in different regimes of turbulent premixed combustion. Proc. Combust. Inst. **38**(2), 2985–2992 (2021)
24. Khan, J.R., Rao, S.: Properties of the turbulent/non-turbulent layer of a turbulent Boussinesq plume: a study using direct numerical simulation. Phys. Fluids **35**(5), 055140 (2023)
25. Ren, J., Wang, H., Luo, K., Fan, J.: Investigation of entrainment and its effect on flame stabilization in a turbulent high Karlovitz number premixed jet flame using direct numerical simulation. Flow, Turbul. Combust. **112**(2), 537–556 (2024)

26. Lee, Y.A., Huisman, S.G., Lohse, D.: Mixing and solvent exchange near the turbulent/non-turbulent interface in a quasi-2D jet. Int. J. Multiphase Flow **169**, 104608 (2023)
27. Horiuti, K.: A classification method for vortex sheet and tube structures in turbulent flows. Phys. Fluids **13**(12), 3756–3774 (2001)
28. Davidson, P.A.: Turbulence: An Introduction for Scientists and Engineers. Oxford Univ, Pr (2004)
29. Horiuti, K., Takagi, Y.: Identification method for vortex sheet structures in turbulent flows. Phys. Fluids **17**(12), 121703 (2005)
30. Kolář, V.: Vortex identification: new requirements and limitations. Int. J. Heat Fluid Flow **28**(4), 638–652 (2007)
31. Nagata, R., Watanabe, T., Nagata, K., da Silva, C.B.: Triple decomposition of velocity gradient tensor in homogeneous isotropic turbulence. Comput. Fluids **198**, 104389 (2020)
32. Liu, C., Gao, Y., Tian, S., Dong, X.: Rortex-A new vortex vector definition and vorticity tensor and vector decompositions. Phys. Fluids **30**(3), 035103 (2018)
33. Kronborg, J., Hoffman, J.: The triple decomposition of the velocity gradient tensor as a standardized real Schur form. Phys. Fluids **35**(3), 031703 (2023)
34. Eisma, J., Westerweel, J., Ooms, G., Elsinga, G.E.: Interfaces and internal layers in a turbulent boundary layer. Phys. Fluids **27**(5), 055103 (2015)
35. Hayashi, M., Watanabe, T., Nagata, K.: Characteristics of small-scale shear layers in a temporally evolving turbulent planar jet. J. Fluid Mech. **920**, A38 (2021)
36. Fiscaletti, D., Buxton, O.R.H., Attili, A.: Internal layers in turbulent free-shear flows. Phys. Rev. Fluids **6**(3), 034612 (2021)
37. Enoki, R., Watanabe, T., Nagata, K.: Statistical properties of shear and nonshear velocity components in isotropic turbulence and turbulent jets. Phys. Rev. Fluids **8**(10), 104602 (2023)
38. Horiuti, K., Fujisawa, T.: The multi-mode stretched spiral vortex in homogeneous isotropic turbulence. J. Fluid Mech. **595**, 341–366 (2008)
39. Watanabe, T., Nagata, K.: Energetics and vortex structures near small-scale shear layers in turbulence. Phys. Fluids **34**(9), 095114 (2022)
40. Pirozzoli, S., Bernardini, M., Grasso, F.: On the dynamical relevance of coherent vortical structures in turbulent boundary layers. J. Fluid Mech. **648**, 325–349 (2010)
41. Vincent, A., Meneguzzi, M.: The dynamics of vorticity tubes in homogeneous turbulence. J. Fluid Mech. **258**, 245–254 (1994)
42. Watanabe, T., Nagata, K.: The response of small-scale shear layers to perturbations in turbulence. J. Fluid Mech. **963**, A31 (2023)
43. Wei, Q., Wang, P., Zheng, X.: Modulations of turbulent/non-turbulent interfaces by particles in turbulent boundary layers. J. Fluid Mech. **983**, A15 (2024)
44. Nakamura, K., Watanabe, T., Nagata, K.: Turbulent/turbulent interfacial layers of a shearless turbulence mixing layer in temporally evolving grid turbulence. Phys. Fluids **35**(4), 045117 (2023)
45. Kankanwadi, K.S., Buxton, O.R.H.: On the physical nature of the turbulent/turbulent interface. J. Fluid Mech. **942**, A31 (2022)
46. Kankanwadi, K.S., Buxton, O.R.H.: Turbulent entrainment into a cylinder wake from a turbulent background. J. Fluid Mech. **905**, A35 (2020)
47. Kohan, K.F., Gaskin, S.J.: On the scalar turbulent/turbulent interface of axisymmetric jets. J. Fluid Mech. **950**, A32 (2022)
48. Chen, J., Buxton, O.R.H.: Spatial evolution of the turbulent/turbulent interface geometry in a cylinder wake. J. Fluid Mech. **969**, A4 (2023)

49. Huang, J., Burridge, H.C., van Reeuwijk, M.: Local entrainment across a TNTI and a TTI in a turbulent forced fountain. J. Fluid Mech. **977**, A13 (2023)
50. Long, Y., Wang, J., Wang, J.: Turbulent/non-turbulent interface in a low-Reynolds-number transitional boundary layer over a multi-element airfoil. Phys. Fluids **34**(10), 102111 (2022)
51. Hiruma, D., Onishi, R., Takahashi, K., Fukagata, K.: Sensitivity study on storm modulation through a strategic use of consumer air conditioners. Atmos. Sci. Lett. **23**(7), e1091 (2022)
52. Mellado, J.P.: Cloud-top entrainment in stratocumulus clouds. Annu. Rev. Fluid Mech. **49**, 145–169 (2017)
53. Nair, V., Heus, T., van Reeuwijk, M.: A lagrangian study of interfaces at the edges of cumulus clouds. J. Atmos. Sci. **78**(8), 2397–2412 (2021)
54. Silva, T.S., Zecchetto, M., da Silva, C.B.: The scaling of the turbulent/non-turbulent interface at high Reynolds numbers. J. Fluid Mech. **843**, 156–179 (2018)
55. Cimarelli, A., Cocconi, G., Frohnapfel, B., De Angelis, E.: Spectral enstrophy budget in a shear-less flow with turbulent/non-turbulent interface. Phys. Fluids **27**(12), 125106 (2015)
56. Morinishi, Y., Lund, T.S., Vasilyev, O.V., Moin, P.: Fully conservative higher order finite difference schemes for incompressible flow. J. Comput. Phys. **143**(1), 90–124 (1998)
57. Rosales, C., Meneveau, C.: Linear forcing in numerical simulations of isotropic turbulence: physical space implementations and convergence properties. Phys. Fluids **17**(9), 095106 (2005)
58. Zecchetto, M., da Silva, C.B.: Universality of small-scale motions within the turbulent/non-turbulent interface layer. J. Fluid Mech. **916**, A9 (2021)
59. Watanabe, T., Zhang, X., Nagata, K.: Turbulent/non-turbulent interfaces detected in DNS of incompressible turbulent boundary layers. Phys. Fluids **30**(3), 035102 (2018)
60. Taveira, R.R., Diogo, J.S., Lopes, D.C., da Silva, C.B.: Lagrangian statistics across the turbulent-nonturbulent interface in a turbulent plane jet. Phys. Rev. E **88**(4), 043001 (2013)
61. Blakeley, B.C., Olson, B.J., Riley, J.J.: Self-similarity of scalar isosurface area density in a temporal mixing layer. J. Fluid Mech. **951**, A44 (2022)